

TinySR: Pruning Diffusion for Real-World Image Super-Resolution

Linwei Dong¹ Qingnan Fan² Yuhang Yu² Qi Zhang²

Jinwei Chen² Yawei Luo^{1†} Changqing Zou^{1,3}

¹Zhejiang University ²Vivo Mobile Communication Co. Ltd ³Zhejiang Lab

Abstract

Real-world image super-resolution (Real-ISR) focuses on recovering high-quality images from low-resolution inputs that suffer from complex degradations like noise, blur, and compression. Recently, diffusion models (DMs) have shown great potential in this area by leveraging strong generative priors to restore fine details. However, their iterative denoising process incurs high computational overhead, posing challenges for real-time applications. Although one-step distillation methods, such as OSEDiff and TSD-SR, offer faster inference, they remain fundamentally constrained by their large, over-parameterized model architectures. In this work, we present **TinySR**, a compact yet effective diffusion model specifically designed for Real-ISR that achieves real-time performance while maintaining perceptual quality. We introduce a **Dynamic Inter-block Activation** and an **Expansion-Corrosion Strategy** to facilitate more effective decision-making in depth pruning. We achieve VAE compression through channel pruning, attention removal and lightweight *SepConv*. We eliminate time- and prompt-related modules and perform pre-caching techniques to further speed up the model. **TinySR** significantly reduces computational cost and model size, achieving up to **5.68×** speedup and **83%** parameter reduction compared to its teacher TSD-SR, while still providing high quality results.

1 Introduction

Real-world image super-resolution (Real-ISR) (Zhang et al. 2021; Wang et al. 2021) aims to reconstruct high-fidelity images from low-quality observations corrupted by compound degradations including noise contamination, nonlinear blur, and compression artifacts. Recently, diffusion models (DMs) have demonstrated significant promise for Real-ISR by leveraging their powerful priors to effectively address complex degradation patterns while recovering realistic textures and details (Ho, Jain, and Abbeel 2020; Nichol and Dhariwal 2021). Their impressive performance over GAN-based Real-ISR methods (Liang, Zeng, and Zhang 2022) has driven their widespread adoption in practical downstream applications. However, for resource-constrained environments, the iterative sampling nature and high computational demands of DMs fundamentally limit their deployment (Chen et al. 2025).

Significant efforts in reducing diffusion model sampling steps have dramatically improved the inference latency of DM-based Real-ISR approaches. Recent advancements in efficient Real-ISR models, such as OSEDiff (Wu et al. 2024a)

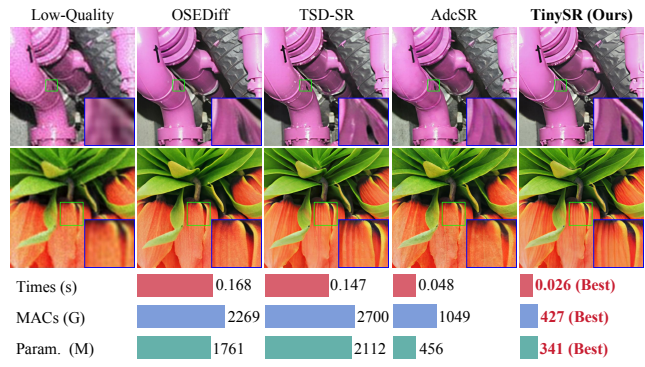


Figure 1: A comprehensive comparison of recent Real-ISR models in terms of visual quality, inference time, computational cost (MACs), and parameter count, highlighting the superior efficiency and performance of our proposed method.

and TSD-SR (Dong et al. 2025) seek to condense the denoising process into a single step by carefully designed distillation while preserving high-quality restoration performance. However, these methods still depend on large pre-trained models, which require significant computational resources and footprint, posing challenges for real-time applications and edge-device deployment. There is a critical demand for more efficient and compact models that can be readily achieved while maintaining competitive performance.

Diffusion compression primarily involves several key techniques, including operator optimization (Dao et al. 2022; Teng et al. 2024), precision quantization (He et al. 2023; Li et al. 2023a), width pruning (Wang et al. 2023; Castells et al. 2024), and depth pruning (Daniel Verdú 2024; Fang et al. 2024). Depth pruning serves as a simple but effective technique, favored for its linear acceleration and straightforward implementation. The conventional paradigm for depth pruning is dependent upon empirical (Kim et al. 2024) or importance-based metrics (Men et al. 2024; Han et al. 2015) to guide layer selection, yet it overlooks the recoverability of the model’s performance on its target task after being pruned. Instead of relying on static importance scores, probability-based mask learning aims to iteratively refine this sampling distribution, such that layers with greater performance recoverability are more likely to be sampled. However,

in ultra-deep networks, mask learning confronts a combinatorial explosion in the search space, which results in prohibitive optimization complexity (Fang et al. 2024).

Beyond deep architecture limitation, DMs-based Real-ISR models exhibit two other computational bottlenecks: high overhead from VAE (Variational Auto-Encoder) and inefficiencies from redundant conditions during super-resolution. AdcSR (Chen et al. 2024a) eliminates the VAE encoder by employing a *PixelUnshuffle* operation (Shi et al. 2016). However, fine-grained channel pruning is required in denoising networks to align channel dimensions, which significantly increases overall complexity and coupling between its components. Regarding prompts and time embeddings, recent studies (Dong et al. 2025; Chen et al. 2024a) indicate that these conditions contribute minimally to the one-step Real-ISR model, suggesting that a more efficient model can be achieved by eliminating these inputs and related modules.

Based on these analyses, we propose **TinySR**, a compact yet effective DMs-based Real-SR model that eliminates computational redundancies in TSD-SR while maintaining restoration quality. Following mask learning, we propose identifying candidate layers that exhibit high-performance recoverability. We partition the network into non-overlapping blocks and introduce sets of learnable probabilities $p(m)$ for each block to constrain search space. We propose **Dynamic Inter-block Activation**, a method that leverages the learnable probability $q(t)$ for soft boundary exploration, and introduce a novel **Expansion-Corrosion Strategy** to determine the optimal pruning scheme. These proposed techniques involve a strategic trade-off between optimization complexity and exploratory potential. Furthermore, we propose several strategies to further compress the Real-ISR model. To lighten the VAE, we perform channel-wise pruning, remove its computationally intensive attention modules, and replace its standard convolutions with depthwise separable convolutions (Howard et al. 2017). We eliminate time- and prompt-related modules to further enhance computational efficiency. Extensive experiments on standard Real-ISR benchmarks demonstrate that our method is up to **5.68 \times** faster, with **84%** MAC and **83%** parameter reductions compared to its teacher, TSD-SR, yet preserves strong perceptual quality (Fig. 1) and comparable quantitative results (Fig. 2).

Overall, our contribution is summarized as follows:

- A Real-ISR model called **TinySR** that achieves **5.68 \times** speedup and **83%** parameter reduction compared to its teacher, while maintaining a strong perceptual quality.
- A novel depth pruning method that incorporates **Dynamic Inter-block Activation** and **Expansion-Corrosion Strategy** to enable more effective pruning decisions.
- Component streamlining strategies incorporate lightweight VAE, redundant conditional structures pruning, and modulation parameters pre-caching.

2 Related Work

Real-World Image Super-Resolution. Real-world image super-resolution (Real-ISR) addresses the challenges of reconstructing high-resolution images from low-quality inputs affected by complex, unknown degradations. Early

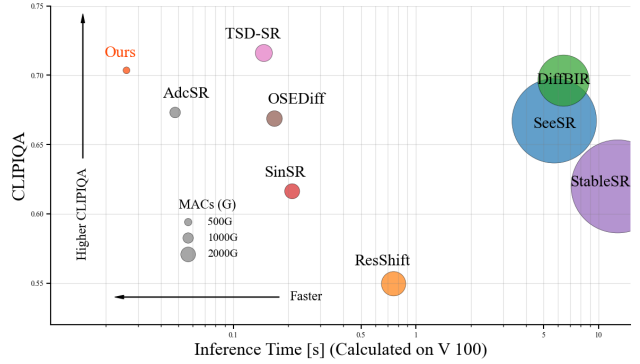


Figure 2: Performance and efficiency comparison among DMs-based Real-ISR methods on an NVIDIA V100 GPU. All metrics are evaluated on the RealSR benchmark. **TinySR** achieves the fastest inference, lightest computation (low MACs) and commendable performance (high CLIPQAs).

approaches like BSRGAN (Zhang et al. 2021) and Real-ESRGAN (Wang et al. 2021) pioneered synthetic degradation modeling using random blur, noise, and compression patterns to enhance generalization. While these methods improved the model’s performance, they often introduced undesirable artifacts. The emergence of diffusion models, particularly Stable Diffusion (Rombach et al. 2022; Esser et al. 2024), marked a significant advancement in perceptual quality. Techniques incorporating StableSR (Wang, Chan, and Loy 2023), DiffBIR (Lin et al. 2023) and SeeSR (Wu et al. 2024b) demonstrated remarkable results in SR tasks, but their iterative denoising process rendered them impractical for time-sensitive applications. Recent efforts have focused on distilling multi-step diffusion processes into efficient one-step networks. Real-ISR methods such as OSEDiff (Wu et al. 2024a) and TSD-SR (Dong et al. 2025) introduced specialized distillation techniques for this purpose. Nevertheless, these models still inherit the substantial computational overhead of their diffusion backbones, with parameter counts often exceeding one billion. This high complexity poses a significant challenge for their deployment on mobile and edge devices.

Efficient Pruning and Compression Techniques. The deployment of large diffusion models on resource-constrained hardware necessitates efficient model compression techniques. TinyFusion (Fang et al. 2024) enables real-time generation by using learnable depth pruning, which is optimized with LoRA-based fine-tuning and Gumbel-Softmax sampling. Other methods, such as BK-SDM (Kim et al. 2024) and SnapFusion (Li et al. 2023b), reduce model size and latency through structural pruning and on-the-fly architecture modification. In the domain of super-resolution, AdcSR (Chen et al. 2024a) introduces an adversarial compression methodology that achieves a $3.7\times$ speedup and a 74% reduction in parameters, while preserving output quality through adversarial distillation. Collectively, these methods represent a substantial advancement in model compression, enabling resource-constrained hardware to generate high-quality outputs with improved computational efficiency.

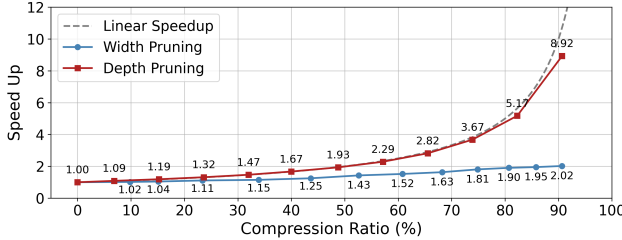


Figure 3: Depth pruning closely aligns with the theoretical linear acceleration curve compared with width pruning.

3 Methodology

We aim to learn a compact but effective diffusion model for real-world image super-resolution (Real-ISR). To mitigate the computational load and inference latency caused by the excessively deep architecture of the TSD-SR network, we prioritize depth pruning (Section 3.1) due to its superior pruning efficiency, as shown in Fig. 3. In Section 3.2, we introduce several key innovations to improve computational efficiency, including a lightweight VAE, a conditional information removal strategy, and a pre-caching technology. Last, the complete training recipes are given in Section 3.3.

3.1 Dynamic Depth Pruning

Depth Pruning Formulation. Consider an N -layers transformer parameterized by $\Phi = [\phi_1, \phi_2, \dots, \phi_N]^T$, where each $\phi_i \in \mathbb{R}^D$. Our goal is to identify an optimal binary mask $m \in \{0, 1\}^N$ that enables effective pruning while maintaining strong Super-Resolution (SR) performance. The pruning mechanism is defined by:

$$x_{i+1} = m_i \cdot \phi_i(x_i) + (1 - m_i) \cdot x_i \quad (1)$$

Here, x_i is the input to the i -th layer, and $\phi_i(x_i)$ is its output. Traditional methods for determining the masking scheme commonly rely on heuristic-based layer importance (e.g., sensitivity analysis) or empirical manual configurations. However, these carefully designed strategies typically overlook the intricate and interdependent layer dynamics within SR diffusion transformers, leading to suboptimal optimization and potentially weak recoverability in the retained layers.

Inspired by TinyFusion (Fang et al. 2024), instead of pursuing models that rely on immediate high-importance feedback, we propose identifying candidate layers with strong recoverability, enabling more efficient teacher-student knowledge distillation. We formalize the pruning process as a bi-level optimization problem:

$$\min_{p(m)} \min_{\Delta\Phi} \mathbb{E}_{x, m \sim \mathcal{G}(p(m))} [\mathcal{L}(x, \Phi + \Delta\Phi, m)] \quad (2)$$

This objective is to identify an optimal mask that minimizes the loss function \mathcal{L} during the optimization process. Since discrete mask selection is non-differentiable, we reparameterize each mask option with a learnable probability parameter $p(m)$ and then use Gumbel-Softmax (Jang, Gu, and Poole 2016) trick \mathcal{G} to do differentiable sampling:

$$\mathcal{G}(p(m)) = \text{one-hot} \left(\frac{\exp((g_i + \log p_i)/\tau)}{\sum_j \exp((g_j + \log p_j)/\tau)} \right) \quad (3)$$

where g_i is random noise drawn from the Gumbel distribution and τ refers to the temperature term. The probabilistic sampling of m can be achieved by $m = \mathcal{G}(p(m))^T \cdot \mathcal{M}$, \mathcal{M} represents the complete search space. For the final pruning decision, we pick m with maximum $p(m)$, as it reveals the strongest recovery. We call this process mask learning.

Search Space Dilemma. A significant challenge in standard mask learning arises from the combinatorial explosion. Let $M : N$ denote the selection of M from N layers, and C_N^M denote the set of combinations. As N grows, pruning 50% will show an explosive trend. For instance, pruning 50% of a 24-layer transformer C_{24}^{12} leads to 2,704,156 possible solutions, making direct probabilistic optimization expensive. Naive approaches address this by partitioning an N -layer network into K non-overlapping blocks of size B , enforcing uniform pruning within each. Assuming statistical independence of the pruning decisions, the total probability $p(m)$ can be factored into the product of local probabilities $p(m^{(j)})$:

$$p(m) = \prod_{j=1}^K p(m^{(j)}) \quad (4)$$

While this simplifies the search, it drastically curtails the space of possible solutions. The cardinality of this feasible subspace, denoted $\mathcal{M}_{\text{valid}}$ is given by:

$$\mathcal{M}_{\text{valid}} = \left\{ m \in \mathcal{M} \mid \forall j \in \{1, \dots, K\}, \sum_{i=(j-1)B+1}^{jB} m_i = s \right\} \quad (5)$$

The accessible fraction of the search space is $\frac{|\mathcal{M}_{\text{valid}}|}{|\mathcal{M}|} = \frac{46,656}{2,704,156} \approx 1.725\%$. This demonstrates that over 98% of all possible pruning masks are rendered unreachable by the imposition of this seemingly innocuous local constraint. Consequently, the true optimal pruning scheme may be inadvertently excluded from this narrowly defined search space.

Dynamic Inter-block Activation. To transcend the limitations of this static partitioning, we introduce a novel pruning framework based on dynamic inter-block activation, as shown in Fig. 4. The core motivation is to relax the rigid local constraints and empower the pruning process to discover its own optimal layer distribution across the network. Instead of confining the search to the highly-constrained $\mathcal{M}_{\text{valid}}$, our method begins within this space yet is allowed to explore beyond it. We achieve this by defining a set of probabilistic transformation operators, T , governed by distribution parameters $q(t)$. Specifically, $T_{j \leftrightarrow h}(m, k)$ transforms m into m' by pruning k active layers from block j (or h) while restoring k layers in h (or j). This mechanism ensures that the total number of active layers remains constant across the pair of blocks (j, h) while dynamically adjusting their individual sparsity profiles. The transformation distribution parameters $q(t)$, are also learnable and applicable to sample a specific scheme through \mathcal{G} . For example, we assume $k = 1, h = j + 1$ and define the option space as $\mathcal{M}' = \{m^-, m, m^+\}$, where m is the pruning mask sampled by $p(m)$, and m^- (resp. m^+) denotes $T_{j \rightarrow j+1}(m, 1)$ (resp. $T_{j \leftarrow j+1}(m, 1)$). The specific

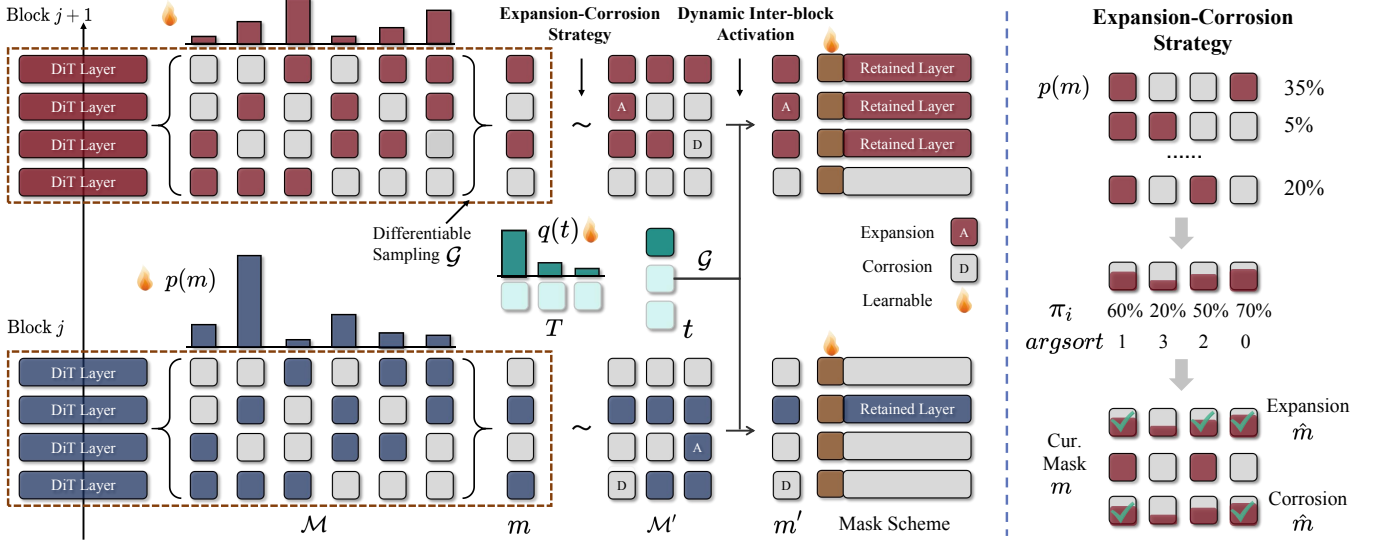


Figure 4: Our proposed mask learning method performs a probability-based decision for candidate solutions, jointly optimized with network weight updates. $p(m)$ characterizes the probability distribution for each block’s pruning scheme. We perform a transformation probability $q(t)$ to facilitate dynamic interaction between masks in different blocks, namely **Dynamic Inter-block Activation**. Leveraging the transfer scheme, we employ an **Expansion-Corrosion Strategy** to determine the final mask by expanding on elements with maximum marginal probability and corroding those with low marginal probability.

mask can be represented as $m' = \mathcal{G}(q(t))^T \cdot \mathcal{M}'$. And the total probability can be expressed as:

$$p(m) = \prod_{j=1}^K \underbrace{p(m^{(j)}) \cdot q(t^{(j)}) \cdot r^{(j)}}_{p(m'^{(j)})} \quad (6)$$

where r is the probability of reaching m through t , and is related to expansion-corrosion strategies.

Expansion-Corrosion Strategy. Instead of random perturbation-based expansion or corrosion, our approach utilizes the maximum marginal probability:

$$\pi_i = p(m_i = 1) = \sum_{m: m_i=1} p(m) \quad (7)$$

which is derived from training priors. Specifically, we start by sorting the values of π_i in descending order. Then we iteratively select candidate layers, corresponding to these sorted values, to form our candidate mask \hat{m} , which is guaranteed to be $|m \vee \hat{m}|_1 - |m|_1 = k$ for expansion and $|m|_1 - |m \wedge \hat{m}|_1 = k$ for erosion. To ensure backpropagation compatibility, we replace the original intersection and union operations with the following simplified computations:

$$m^- = m \odot \hat{m}, \quad m^+ = \text{clamp}(m + \hat{m}, 0, 1) \quad (8)$$

Here, \odot represents the element-wise product. This continuous relaxation maintains the meaning of expansion or corrosion while allowing for gradient flow, which is crucial for training.

Pruning Decision. Unlike traditional mask learning, where decisions are made directly from $p(m)$, our approach determines the transformations for each block based on maximum $q(t)$ and then selects the final mask based on π .

3.2 Component Streamlining

Efficient VAE Architecture. We identify three primary performance bottlenecks in the VAE of the TSD-SR framework: 1) Excessively large channel dimensions. As shown in Fig. 6(a), the MACs of components exhibit significant and widely varying reductions after pruning, particularly across compute-intensive modules such as the down, up and mid blocks. 2) Computationally intensive attention mechanisms. As shown in Fig. 6(b), compared to the resnet block, the attention block poses a more significant computational bottleneck, primarily due to its considerably higher MAC count. 3) Time-consuming standard convolution. Convolutional operations are computationally dominant within the VAE, constituting more than 85% of the overall computational workload. To address the above problem, we perform pruning on both the encoder and decoder. Specifically, following (Bohan 2023), we first prune the maximum channel width to 64 throughout the network, substantially reducing both parameter count and computational complexity. All self-attention modules are subsequently removed from the architecture to mitigate their substantial computational expense. To better accommodate higher compression rates, we integrate depthwise separable convolutions (Howard et al. 2017; Chollet 2017) into the encoder. However, the same modification proves detrimental to the decoder’s performance, leading us to restrict the use of lightweight convolutions to the encoder alone.

Pruning Redundant Conditional Structures. In the TSD-SR model (our teacher), prompt embeddings, essential for text-to-image generation, contribute minimally to image SR tasks (Fig. 7), as it uses the default prompt embedding. Similarly, the time embedding layers, crucial for multi-step diffusion, are redundant in single-step SR and can be removed to

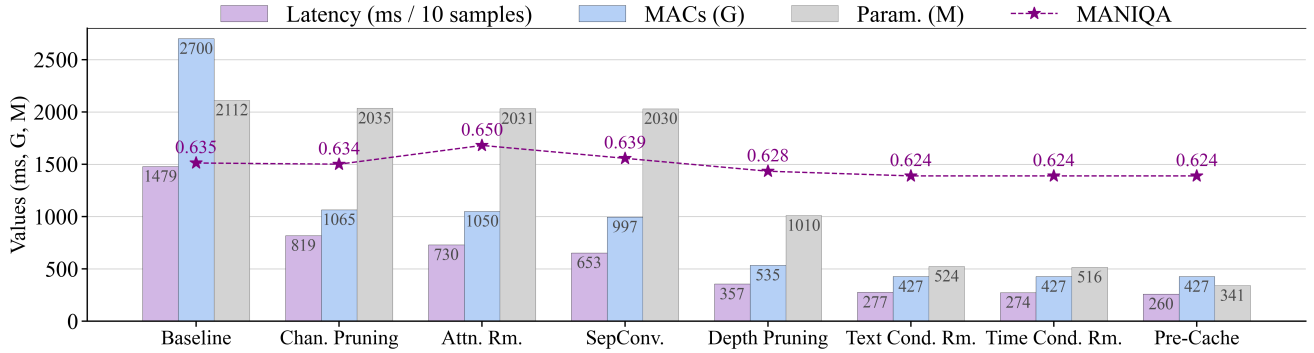


Figure 5: Comparisons of performance and efficiency for various design of efficient TinySR. Quality is measured by the MANIQA score, calculated on RealSR dataset. Efficiency is assessed via latency, MACs, and parameters. Latency and MACs are benchmarked for super-resolution a 128×128 low-quality image on a n NVIDIA V100 GPU. Our model achieves a **5.68** \times acceleration with **83%** fewer parameters and **84%** lower MACs, while maintaining comparable quality to the baseline.

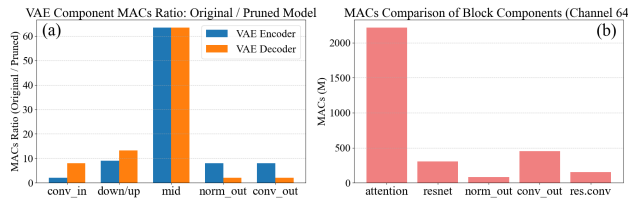


Figure 6: Left: Channel pruning effectively reduces MACs across all modules, particularly in the computationally intensive down/up and middle blocks. Right: Attention mechanism dominates the computational cost in a 64-channel VAE.

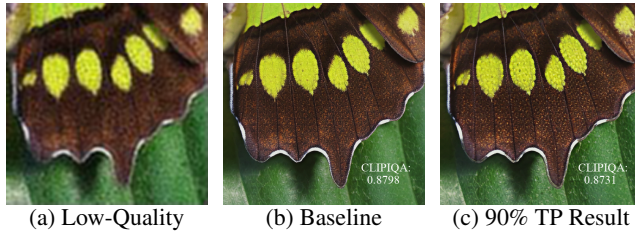


Figure 7: Applying 90% token pruning (TP) yields visually comparable results to the baseline with a slight quality drop, indicating the limited contribution of the default prompt.

reduce computational cost without affecting output quality.

Pre-cache Modulation Param. In TSD-SR architecture, shift and scale parameters are generated by adaLN-Zero modulation (Esser et al. 2024; Peebles and Xie 2023). A key finding is that these modulation parameters generated by our model stabilize post-training and no longer exhibit input dependency. This property enables us to pre-compute and cache these parameters, which are then loaded for inference, leading to a significant reduction in computational overhead.

With all these optimizations, our compact model achieves **83%** fewer parameters and **84%** lower MACs but with com-

parable quality and **5.68** \times acceleration, as shown in Fig. 5.

3.3 Training Scheme

VAE Training. The Tiny encoder aligns with the teacher’s latent representations using MSE loss, and the Tiny decoder is regularized by LPIPS and GAN losses to improve the fidelity and perceptual quality of the reconstructed images.

Pruning Decision Training. To ensure the recoverability of pruning, we design the optimization of mask learning using distillation and task loss. Specifically, distillation loss is defined as L_1 loss and task loss is defined as LPIPS loss.

Restoration Training. A two-stage training approach is utilized to expedite model convergence. The first stage involves latent space training with a distillation loss for efficient feature alignment. The second stage then adds LPIPS and GAN losses in the pixel space to improve image-level fidelity.

Comprehensive experimental details for the training procedure are available in the supplementary material.

4 Experiments

4.1 Experimental Settings

Datasets. We utilize DIV2K (Agustsson and Timofte 2017), Flickr2K (Timofte et al. 2017), LSDIR (Li et al. 2023c), and FFHQ (Karras, Laine, and Aila 2019) for training. To synthesize low-resolution and high-resolution image pairs, we employ the same degradation pipeline as described in Real-ESRGAN (Wang et al. 2021). We evaluate the performance of our model on the synthetic DIV2K-Val (Agustsson and Timofte 2017) dataset, alongside two real-world datasets, RealSR (Cai et al. 2019) and DRealSR (Wei et al. 2020). The datasets consist of paired images with 128x128 low-quality and 512x512 high-quality resolutions.

Evaluation Metrics. For evaluating our method, we apply both full-reference and no-reference metrics. Full-reference metrics include PSNR and SSIM (Wang et al. 2004) (calculated on the Y channel in YCbCr space) for fidelity, LPIPS

Table 1: Quantitative comparison of various methods on the DIV2K-Val dataset, with all efficiency metrics benchmarked on a NVIDIA V100 GPU. The best and second-best results are highlighted in **bold**, *italic*, respectively.

Method	SSIM \uparrow	LPIPS \downarrow	DISTS \downarrow	FID \downarrow	NIQE \downarrow	MUSIQ \uparrow	CLIPQA \uparrow	#Steps	Time (s)	MACs (G)	#Param. (M)
StableSR	0.5722	0.3111	0.2046	24.95	4.7737	65.78	0.6764	200	12.731	79940	1410
DiffBIR	0.5717	0.3469	0.2108	33.93	4.6056	68.54	0.7125	50	6.435	24234	1717
SeeSR	0.6057	0.3198	0.1953	25.81	4.8322	68.49	0.6899	50	5.722	65857	2524
ResShift	0.6234	0.3473	0.2253	42.01	6.3615	60.63	0.5962	15	0.755	5491	174
SinSR	0.6018	0.3262	0.2069	35.55	5.9981	62.95	0.6501	1	0.210	2095	174
OSEDiff	<i>0.6109</i>	0.2942	0.1975	26.34	4.7089	67.31	0.6681	1	0.168	2269	1761
AdcSR	0.6017	0.2853	0.1899	25.52	4.3580	68.00	0.6764	1	0.048	1049	456
TSD-SR	0.5808	0.2673	0.1821	29.16	4.3224	71.69	0.7416	1	0.147	2700	2112
Ours	0.5725	0.2793	0.1883	22.44	4.1500	69.90	0.7201	1	0.026	427	<i>341</i>

(Zhang et al. 2018) and DISTS (Ding et al. 2020) for perceptual quality, and FID (Heusel et al. 2017) for distribution comparison. No-reference metrics include NIQE (Zhang, Zhang, and Bovik 2015), MUSIQ (Ke et al. 2021), MANIQA (Yang et al. 2022), CLIPQA (Wang, Chan, and Loy 2023), TOPIQ (Chen et al. 2024b) and Q-Align (Wu et al. 2023).

4.2 Comparison with Existing SR Methods

We categorize existing outstanding SR models into two groups, single-step and multi-step diffusion models. Single-step models include SinSR (Wang et al. 2024b), OSEDiff (Wu et al. 2024a), TSD-SR (Dong et al. 2025), and AdcSR (Chen et al. 2024a), and multi-step models include StableSR (Wang et al. 2024a), DiffBIR (Lin et al. 2023), SeeSR (Wu et al. 2024b), and ResShift (Yue, Wang, and Loy 2024). Additional details of GAN-based Real-ISR methods (Zhang et al. 2021; Chen et al. 2022; Liang, Zeng, and Zhang 2022; Wang et al. 2021) are given in the supplementary material.

Quality Comparison. Tab. 1 shows a comparison with DMs-based baselines in Real-ISR tasks. For the first four full-reference metrics, our model achieves performance comparable to its teacher TSD-SR and outperforms most other models, securing the second rank for LPIPS and DISTS. Furthermore, our model achieves the best result for the distribution metric FID. For the latter three no-reference metrics, it demonstrates competitive performance: outperforming all other models for NIQE, and ranking second for both MUSIQ and CLIPQA, thereby surpassing most other methods.

As illustrated in Fig. 1 and Fig. 8, **TinySR** achieves competitive performance in recovering high-quality, sharp, and photorealistic images. Visual artifacts, specifically the generation of fake textures, are frequently observed in outputs from multi-step models such as StableSR, SeeSR, DiffBIR, and ResShift due to their propensity for over-generation. A clear example, demonstrated in Fig. 8 (top), is the spurious generation of hair patterns in regions where they should not exist. OSEDiff and AdcSR consistently demonstrate suboptimal restoration performance, frequently yielding outputs with discernible blur. While TSD-SR exhibits excellent generation capabilities, it also tends to produce fake textures, as shown in Fig. 8 (bottom). **TinySR**, by contrast, demonstrates robust capabilities in reconstructing natural textures, notably encompassing structural integrity, botanical patterns, and sculpted surface details.

Table 2: Performance comparison of depth pruning methods on the DIV2K-Val dataset. Our method exhibits superior recovery performance relative to other pruning strategies.

Method	DISTS \downarrow	FID \downarrow	MANIQA \uparrow	CLIPQA \uparrow	TOPIQ \uparrow	Q-Align \uparrow
Random-Min.	0.2012	31.40	0.5629	0.6944	0.6314	3.5698
Flux-Lite	0.2001	30.36	0.5822	0.6983	0.6529	3.6312
ShortGPT	0.2034	32.45	0.5681	0.7116	0.6584	3.6110
Sensitivity	0.1914	26.25	0.5879	0.6900	0.6583	3.7135
SnapFusion	0.2018	31.18	0.5788	0.7112	0.6579	3.6468
BK-SDM	0.1974	29.27	0.5792	0.6985	0.6562	3.6466
TinyFusion	0.1904	26.46	0.5880	0.6995	0.6580	3.7301
Ours	0.1883	22.44	0.6083	0.7201	0.6629	3.7774

Efficiency Comparison. As demonstrated by the last four columns of Tab. 1, the proposed TinySR exhibits superior efficiency in terms of step number, inference time, and computational cost. By leveraging one-step inference and advanced compression, our model achieves dramatic efficiency gains over leading multi-step Real-ISR methods while maintaining comparable performance. Compared to StableSR, SeeSR, DiffBIR, and ResShift, our model delivers significant speed improvements ($489\times$, $220\times$, $247\times$, $29\times$) with corresponding MAC reductions ($187\times$, $154\times$, $57\times$, and $12\times$). Compared to the one-step model SinSR and OSEDiff, it achieves $8.1\times$ and $6.4\times$ acceleration, respectively. Compared to its teacher, TSD-SR, it achieves a $5.68\times$ acceleration, a 84% reduction in computation, and a 83% decrease in total parameters, as shown in Fig. 5. Notably, In a direct comparison with the current state-of-the-art SR compression model, AdcSR, our model also demonstrates superior efficiency, with a $1.8\times$ speedup and a $2.45\times$ computation reduction.

4.3 Comparison with Depth Pruning Methods

We evaluate the depth pruning methods following these baselines: (1) Perturbation-based – We randomly prune models and select one with minimal task loss (LPIPS) for training; (2) Similarity-based – Typically, these methods base their decisions on an analysis of the similarity between each layer’s input and output, such as Flux-Lite (Daniel Verdú 2024) and ShortGPT (Men et al. 2024); (3) Metric-based – Decision-making through metric in general, such as Sensitivity Analysis (Han et al. 2015) and SnapFusion (Li et al. 2023b). (4) Experience-based - We follow the design of BK-SDM (Kim et al. 2024) for corresponding pruning; (5) Probability-based – Decision by optimized probability parameters, such

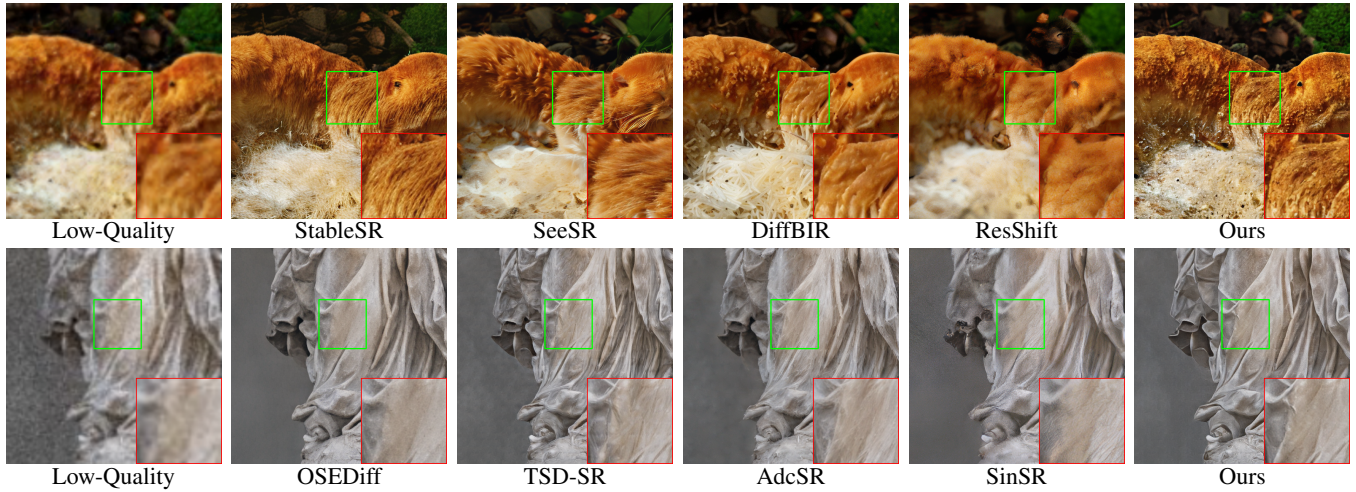


Figure 8: Qualitative comparisons of different DMs-based Real-ISR methods. Please zoom in for a better view.

as TinyFusion (Fang et al. 2024) and our method. Randomly generating and then selecting the minimum loss yields a low initial loss, but exhibits extremely weak recovery ability after training. Similarity-based methods demonstrate suboptimal fidelity (poor DISTs) and pronounced inconsistencies across various no-reference metrics. For example, ShortGPT performs well on CLIPQA but struggles considerably on MANIQA. Metric-based methods often exhibit a bias towards the metrics they optimize. For instance, while Sensitivity Analysis performs well on reference metrics, and SnapFusion excels on CLIPQA due to its pruning scheme’s relation to it, both approaches demonstrate shortcomings in other metrics. Although BK-SDM and TinyFusion show some effectiveness, our method exhibits enhanced recoverability over all other approaches, performing favorably across both full-reference and no-reference evaluation metrics.

4.4 Ablation Study

Effect of VAE Compression. Tab. 3 presents the ablation studies of VAE compression process. Channel pruning offers a significant reduction in computational overhead, with only a minor compromise to perceptual reconstruction fidelity. While removing the attention module effectively doubles inference speed, it can somewhat impact reconstruction quality. For lightweight convolution, an alternative approach, employing SnapGen’s (Chen et al. 2025) strategy of expanding channels in *SepConv* intermediate layers, yields performance comparable to our proposed solution. However, our method notably exhibit reduced computational overhead and superior inference efficiency. Our efforts culminated in a lightweight VAE that delivers reconstruction quality on par with the teacher, concurrently achieving a $10\times$ increase in inference speed and a $22\times$ reduction in MACs.

Effect of Removing the Text and Time Modules. Tab. 4 presents the ablation study on the elimination of text and time conditions, which demonstrates that our approach achieves a highly favorable trade-off between efficiency and quality. Excising the text embeddings and related context modules

Table 3: Ablation study of VAE compression on DrealSR.

Method	PSNR \uparrow	SSIM \uparrow	LPIPS \downarrow	Time(ms)	MACs(G)
Tea. VAE	27.77	0.7559	0.2967	95.36	1781.91
+ Chan. Pruning	27.49	0.7544	0.3052	22.79	146.56
+ Rm. Attn.	27.36	0.7420	0.3222	11.22	131.91
SnapGen SepConv	27.50	0.7497	0.3054	10.75	89.74
Ours	27.56	0.7514	0.3038	9.25	78.48

Table 4: Ablation study of removing the text embeddings, time embeddings, and related modules on RealSR.

Method	CLIPQA \uparrow	MANIQA \uparrow	Time (ms)	MACs(G)	#Param. (M)
w/ Text & Time	0.7081	0.6283	35.7	535	1010
Ours	0.7035	0.6235	27.4	427	516

yields a 486M parameter, 108G MACs, and 8ms time reduction, while only marginally decreasing the CLIPQA score by 0.0046 and the MANIQA score by 0.0048. Subsequent removal of the time modules further reduces parameters by 8M with a negligible impact on reconstruction quality. Given these results, these modules are omitted from our final design.

5 Conclusion

In this paper, we propose **TinySR**, a highly efficient model that incorporates several novel contributions. For depth pruning, we introduce a **Dynamic Inter-block Activation** mechanism and an **Expansion-Corrosion Strategy** to facilitate mask learning optimization. These proposed techniques involve a strategic trade-off between optimization complexity and exploratory potential. To further reduce computational load, we compress the VAE via channel pruning, attention module removal, and the use of lightweight *SepConv*. Finally, we accelerate inference by eliminating time- and prompt-conditioning modules and implementing pre-caching techniques. Consequently, **TinySR** achieves up to a **5.68 \times** speedup and a **83%** parameter reduction compared to its teacher, TSD-SR, while maintaining high-quality results.

Supplementary Material

A Implementation Details

Data Processing. Following (Wu et al. 2024a; Chen et al. 2024a; Dong et al. 2025; Wu et al. 2024b), the super-resolution process is conducted with a scale factor of 4, up-sampling images from 128×128 to 512×512 . To create the degraded dataset, Ground Truth (GT) images are first randomly cropped from their original sources. Subsequently, these GT images are synthesized into 128×128 degraded data via the well-established Real-ESRGAN (Chen et al. 2022) degradation pipeline, involving various corruptions such as noise, blurring, and compression. This data processing method is widely adopted and well-established. (Wang et al. 2024a; Xie et al. 2024; Yue, Wang, and Loy 2024; Wang et al. 2024b). Moreover, to minimize memory overhead and accelerate training, we pre-encode the low-quality, high-quality, and teacher-generated references into the VAE’s latent representations. These latent representations are then cached, enabling their swift retrieval during the training phase.

VAE Training. For the standard Teacher VAE, we first reduce the number of channels in all intermediate layers to 64 and remove all attention mechanisms, following (Bohan 2023). Subsequently, all standard convolutional layers are substituted with depthwise separable convolutions (*SepConv*), in line with the methodology proposed by (Howard et al. 2017; Chollet 2017).

We train the VAE encoder \mathcal{E}_{tiny} by aligning latent space features using MSE loss. The training objective is defined as:

$$\mathcal{L}_{encoder} = \|\mathcal{E}_{tiny}(x_{LR}) - \mathcal{E}_{pre}(x_{LR})\|_2^2 \quad (A.1)$$

Here, x_{LR} represents low-quality data, \mathcal{E}_{pre} is the pre-trained encoder. Training is conducted for 100k steps using a batch size of 64 and a learning rate (AdamW optimizer) of 3e-4 for this phase.

We use LPIPS loss and GAN loss to train the VAE decoder \mathcal{D}_{tiny} :

$$\begin{aligned} \mathcal{L}_{decoder} = & \lambda_1 \mathcal{L}_{LPIPS}(\mathcal{D}_{tiny}(\mathcal{E}_{pre}(x_{LR})), x_{HR}) \\ & + \lambda_2 \mathcal{L}_{GAN}(\mathcal{D}_{tiny}(\mathcal{E}_{pre}(x_{LR}))) \end{aligned} \quad (A.2)$$

Here, x_{HR} represents high-quality data. We set λ_1 to 3 and λ_2 to 1. We employ a learning rate of 5e-4 for the decoder and 1e-5 for the discriminator during training. We train the model for 200k iterations using 64 batch size setting. The random seed is set to 80 throughout the training.

Pruning Decision Training. We initialize our model using the pre-trained weights of TSD-SR (Dong et al. 2025) for pruning training. We set the pruning rate to 50% to establish our baseline model. Following the TinyFusion (Fang et al. 2024) approach, we retained two out of every four layers and employed a dynamic block-wise activation mechanism between adjacent layers. Our masks are calculated via the Gumbel-Softmax operation (Jang, Gu, and Poole 2016). During network propagation, calculation for a layer is bypassed if its associated mask value is 0. We optimize the network and probability parameters using SR’s task loss and distillation loss aligned with the teacher features. Specifically, task

loss is defined as LPIPS loss and L_1 loss is utilized for the distillation loss. The total loss is expressed as follows:

$$\begin{aligned} \mathcal{L}_{pruning} = & \lambda_3 \mathcal{L}_{LPIPS}(\mathcal{D}_{tiny}(z_{stu}), x_{HR}) \\ & + \lambda_4 \|z_{stu} - z_{tea}\|_1 \\ \text{where } z_{stu} \sim & x_{LR} - \epsilon_{stu}(\mathcal{E}_{tiny}(x_{LR}), t), \\ z_{tea} \sim & x_{LR} - \epsilon_{tea}(\mathcal{E}_{tea}(x_{LR}), t) \end{aligned} \quad (A.3)$$

ϵ_{stu} denotes the student’s denoising network, while ϵ_{tea} represents the teacher’s. t denotes timesteps, and \mathcal{E}_{tea} denotes the teacher encoder. This encoder differs from the pre-trained version \mathcal{E}_{pre} as it is fine-tuned by TSD-SR (Dong et al. 2025).

Training is conducted for 100k iterations across 8 NVIDIA V100 GPUs, employing a learning rate of 5e-5 (AdamW optimizer) and a global batch size of 8. We use LoRA training, with LoRA rank set to 64. λ_3 and λ_4 are both set to 1.

Restoration Training. We perform depth pruning on the TSD-SR according to the pruning mask and discard the condition-related components to initialize our student network. To achieve rapid convergence, we divided the model’s training into two stages. In the first stage, training is exclusively conducted within the latent space. We employ L_1 loss for teacher-student knowledge distillation to align features. The formulation of this distillation loss is consistent with that described in Eq. (A.3):

$$\mathcal{L}_{stage_1} = \|z_{stu} - z_{tea}\|_1 \quad (A.4)$$

The meaning of z_{stu} and z_{tea} is the same as mentioned above. Training in the latent space enables us to use a larger global batch size (128) on 8 V100 GPUs. We set the learning rate to 1e-4 and the LoRA rank to 64. We iterate training 150k steps until convergence.

In stage 2, we further enhance the perceptual quality of the results in image space by fine-tuning the model directly within the image domain. We additionally incorporate LPIPS loss and GAN loss to enhance image restoration. The total loss is expressed as follows:

$$\begin{aligned} \mathcal{L}_{stage_2} = & \lambda_5 \|z_{stu} - z_{tea}\|_1 \\ & + \lambda_6 \mathcal{L}_{LPIPS}(\mathcal{D}_{tiny}(z_{stu}), x_{HR}) \\ & + \lambda_7 \mathcal{L}_{GAN}(\mathcal{D}_{tiny}(z_{stu})) \end{aligned} \quad (A.5)$$

The meaning of z_{stu} , z_{tea} and \mathcal{D}_{tiny} is the same as mentioned above. λ_5 , λ_6 , and λ_7 are set to 5, 1, and 0.3, respectively. We fine-tune our model for 50k steps on 8 V100 GPUs, with a global batch size of 96, a learning rate of 1e-6 for student (5e-6 for discriminator), and a LoRA rank of 64. The random seed for the entire training process is set to 80. And all training is done on *fp16* precision.

B More Comparisons on Benchmarks

B.1 More Quantitative Comparisons

We compared GAN-based and diffusion-based methods across various datasets (DIV2K-Val (Agustsson and Timofte 2017), DrealSR (Wei et al. 2020), RealSR (Cai et al. 2019)), with the results presented in Tab. A.1. We observe that traditional GAN-based approaches (Zhang et al. 2021; Chen et al. 2022; Liang, Zeng, and Zhang 2022; Wang et al.

Table A.1: Quantitative comparison among different GAN-based and diffusion-based Real-ISR approaches on both synthetic and real-world benchmarks. “s” denotes the required number of sampling steps in the diffusion-based method. The best and second-best results are highlighted in **bold**, *italic*, respectively

Dataset	Method	PSNR \uparrow	SSIM \uparrow	LPIPS \downarrow	DISTS \downarrow	FID \downarrow	NIQE \downarrow	MUSIQ \uparrow	MANIQA \uparrow	CLIP IQA \uparrow
DIV2K-Val	BSRGAN	24.58	0.6269	0.3502	0.2280	49.55	4.75	61.68	0.5071	0.5386
	Real-ESRGAN	24.02	0.6387	0.3150	0.2123	38.87	4.83	61.06	0.5401	0.5251
	LDL	23.83	<i>0.6344</i>	0.3256	0.2227	42.29	4.86	60.04	0.5350	0.5180
	FeMASR	23.06	0.5887	0.3126	0.2057	35.87	4.74	60.83	0.5074	0.5997
	StableSR-s200	23.27	0.5722	0.3111	0.2046	24.95	4.77	65.78	0.6164	0.6764
	DiffBIR-s50	23.13	<i>0.5717</i>	0.3469	0.2108	33.93	4.61	68.54	0.6360	0.7125
	SeeSR-s50	23.73	0.6057	0.3198	0.1953	25.81	4.83	68.49	<i>0.6198</i>	0.6899
	ResShift-s15	24.71	0.6234	0.3473	0.2253	42.01	6.36	60.63	0.5283	0.5962
	SinSR-s1	24.41	0.6018	0.3262	0.2069	35.55	6.00	62.95	0.5430	0.6501
	OSEDiff-s1	23.72	0.6109	0.2942	0.1975	26.34	4.71	67.31	0.6131	0.6681
	AdcSR-s1	23.74	0.6017	0.2853	0.1899	25.52	4.36	68.00	0.6090	0.6764
	TSD-SR-s1	23.02	0.5808	0.2673	0.1821	29.16	4.32	71.69	0.6192	0.7416
	TinySR-s1 (Ours)	22.76	0.5725	0.2793	0.1883	24.44	4.15	69.90	0.6083	0.7201
DRealSR	BSRGAN	28.70	0.8028	0.2858	0.2143	155.61	6.54	57.15	0.4847	0.5091
	Real-ESRGAN	28.61	<i>0.8051</i>	0.2818	0.2088	147.66	6.70	54.27	0.4888	0.4512
	LDL	28.20	0.8124	0.2791	0.2127	155.51	7.14	53.94	0.4894	0.4476
	FeMASR	26.87	0.7569	0.3156	0.2238	157.72	5.91	53.70	0.4413	0.5633
	StableSR-s200	28.04	0.7454	0.3279	0.2272	144.15	6.60	58.53	0.5603	0.6250
	DiffBIR-s50	25.93	0.6525	0.4518	0.2761	177.04	6.23	65.66	0.6296	0.6860
	SeeSR-s50	28.14	0.7712	0.3141	0.2297	146.95	6.46	64.74	0.6022	0.6893
	ResShift-s15	28.69	0.7874	0.3525	0.2541	176.77	7.88	52.40	0.4756	0.5413
	SinSR-s1	28.38	0.7499	0.3669	0.2484	172.72	6.96	55.03	0.4904	0.6412
	OSEDiff-s1	27.92	0.7836	0.2968	0.2162	135.51	6.45	64.69	0.5898	0.6958
	AdcSR-s1	28.10	0.7726	0.3046	0.2200	134.05	6.45	66.26	0.5927	0.7049
	TSD-SR-s1	27.77	0.7559	0.2967	0.2136	134.98	5.91	66.62	0.5874	0.7344
	TinySR-s1 (Ours)	27.48	0.7459	0.3116	0.2204	146.70	5.67	65.36	0.5804	0.7094
RealSR	BSRGAN	26.38	0.7651	0.2656	0.2121	141.24	5.64	63.28	0.5425	0.5114
	Real-ESRGAN	26.65	0.7603	0.2726	0.2065	136.29	5.85	60.45	0.5507	0.4518
	LDL	25.28	0.7565	0.2750	0.2119	142.74	5.99	60.92	0.5494	0.4559
	FeMASR	25.07	0.7356	0.2936	0.2285	141.01	5.77	59.05	0.4872	0.5405
	StableSR-s200	24.62	0.7041	0.3070	0.2156	128.54	5.78	65.48	0.6223	0.6198
	DiffBIR-s50	24.24	0.6650	0.3469	0.2300	134.56	5.49	68.35	0.6544	0.6961
	SeeSR-s50	25.21	0.7216	0.3003	0.2218	125.10	5.40	69.69	<i>0.6443</i>	0.6671
	ResShift-s15	26.39	0.7567	0.3158	0.2432	149.59	6.87	60.22	0.5419	0.5496
	SinSR-s1	26.27	0.7351	0.3217	0.2341	137.59	6.30	60.76	0.5418	0.6163
	OSEDiff-s1	25.15	0.7341	0.2920	0.2128	123.48	<i>5.65</i>	69.10	0.6326	0.6687
	AdcSR-s1	25.47	0.7301	0.2885	0.2129	118.41	5.35	69.90	0.6360	0.6731
	TSD-SR-s1	24.81	0.7172	0.2743	0.2104	114.45	<i>5.13</i>	71.19	0.6347	0.7160
	TinySR-s1 (Ours)	24.79	0.7171	0.2806	0.2123	118.00	4.74	69.78	0.6235	0.7035

2021) generally excel on full-reference metrics, particularly PSNR and SSIM. However, some studies indicate that PSNR and SSIM often do not accurately reflect fidelity under more complex degradation conditions (Xie et al. 2024; Dong et al. 2025; Yu et al. 2024). In most perceptual quality metrics, such as NIQE (Zhang, Zhang, and Bovik 2015), MUSIQ (Ke et al. 2021), MANIQA (Yang et al. 2022) and CLIP-IQA (Wang, Chan, and Loy 2023), diffusion-based methods demonstrate superior performance compared to these GANs, highlighting their enhanced capability in generating natural textures. TinySR achieved competitive performance across most metrics, demonstrating comparable results to its teacher model, TSD-SR, and showcasing the robust recoverability of the pruning methods.

B.2 More Qualitative Comparisons

Fig. B.1 presents a visual comparison between the GAN-based and diffusion-based methods. GAN-based methods of

ten struggle to recover fine, high-frequency details, resulting in blurred textures. For instance, models such as BSRGAN, Real-ESRGAN, LDL, and FeMASR produce blurring on petal textures. Similarly, BSRGAN and LDL create overly smooth butterfly wings, while Real-ESRGAN and FeMASR fail to reconstruct crisp mushroom textures. This consistent lack of detail suggests a fundamental limitation in the ability of these GAN-based approaches to restore high-frequency information. Multi-step diffusion-based methods, such as StableSR, DiffBIR, SeeSR, and ResShift, can introduce artifacts when restoring natural textures like water and rocks, and may also produce blurred details. Notably, DiffBIR is particularly susceptible to over-generation, which can result in illogical or unnatural textures, as has been observed in the restoration of images containing mushrooms. Methods like OSEdiff, AdcSR, and SinSR can suffer from incomplete denoising and are prone to generating broken or fragmented textures during the super resolution process. Our model demonstrates

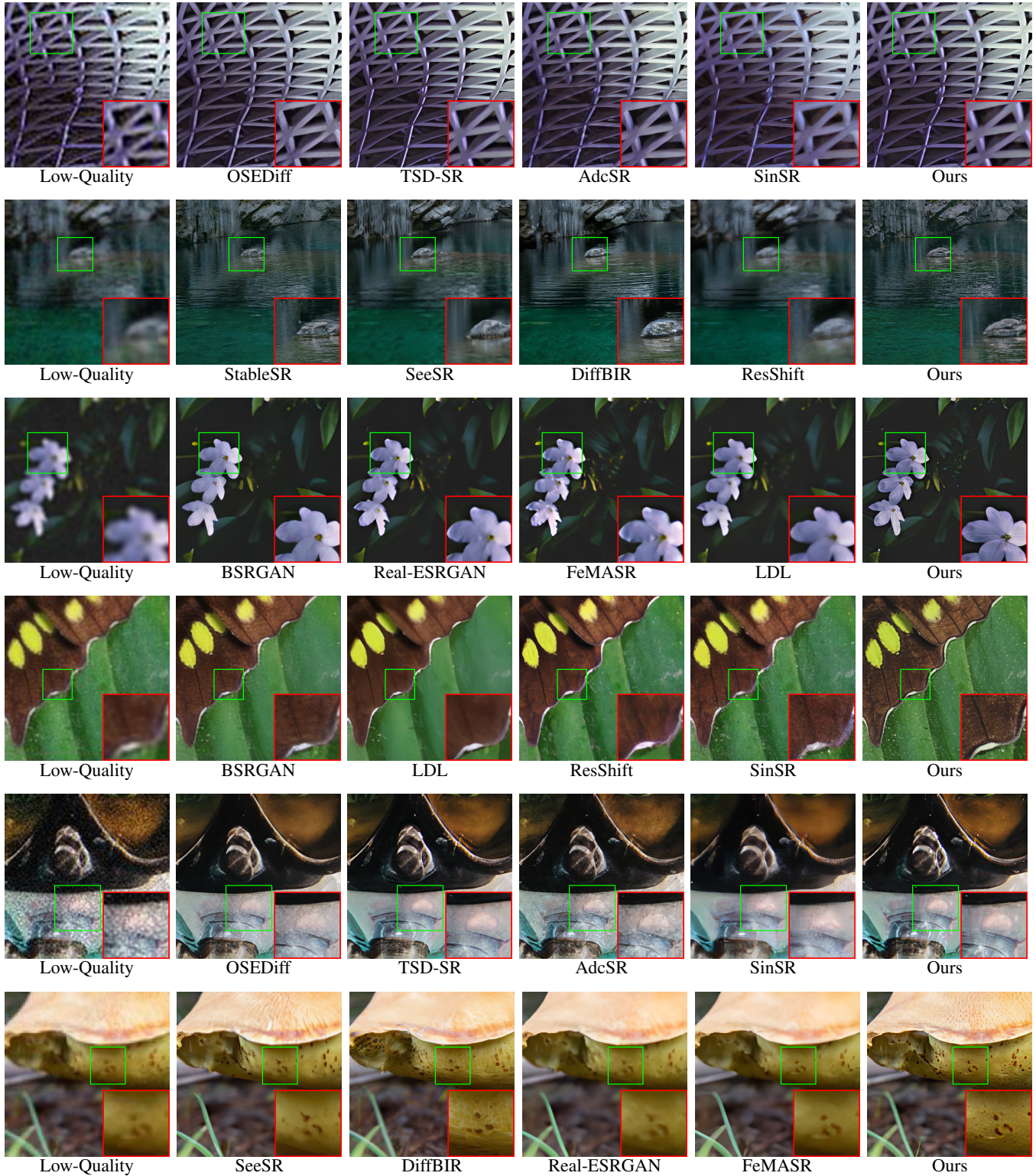


Figure B.1: Qualitative comparisons of GAN-based and diffusion-based Real-ISR methods. Please zoom in for a better view.

highly competitive performance, excelling in both structural and texture recovery. Compared to other methods, it restores

a greater degree of high-frequency detail while rigorously maintaining overall structural integrity.

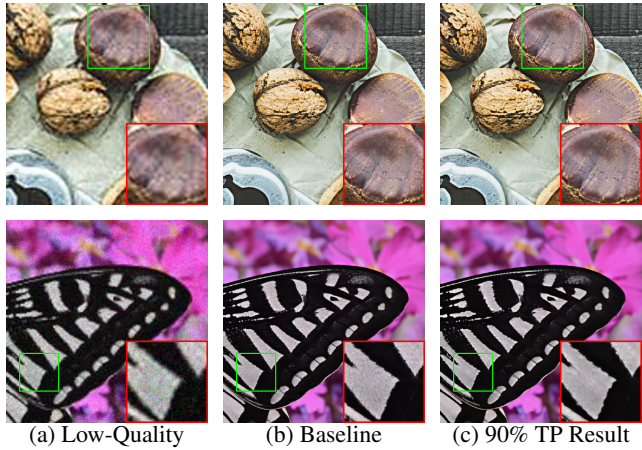


Figure C.1: Applying 90% token pruning (TP) yields visually comparable results to the baseline with a slight quality drop, indicating the limited contribution of the default prompt.

Table C.1: Ablation study of prompt token pruning (TP) on DrealSR dataset. The best is highlighted in **bold**.

Method	PSNR \uparrow	LPIPS \downarrow	DISTS \downarrow	NIQE \downarrow	MUSIQ \uparrow	MANIQA \uparrow
Baseline	27.77	0.2967	0.2136	5.9131	66.62	0.5927
TP 10% token	27.66	0.2945	0.2135	5.9536	66.57	0.5870
TP 25% token	27.65	0.2947	0.2135	5.9510	66.53	0.5861
TP 50% token	27.66	0.2924	0.2120	5.9350	66.35	0.5801
TP 75% token	27.62	0.2860	0.2122	6.0142	65.79	0.5783
TP 90% token	27.59	0.2866	0.2144	6.1461	65.01	0.5721

C More Ablation Studies.

C.1 Ablation Study on Prompt Condition

Tab. C.1 presents the results of token pruning of the teacher model. We found that pruning prompt information does not negatively impact certain full-referenced metrics. In fact, some metrics, such as LPIPS and DISTS, even show improvement at specific pruning rates. Token pruning primarily affects no-referenced metrics. However, we observe no significant performance degradation even at a 50% pruning ratio. Furthermore, performance degrades gracefully at higher pruning percentages without a sharp decline, which suggests that the contribution of textual information to the final image synthesis is limited. As shown in Fig. C.1, although TP 90% token’s output contains less fine-grained detail than the baseline, it effectively removes the noise from the low-quality input, resulting in an image with high visual quality.

C.2 Ablation Study on Pruning Ratio

Tab. C.2 compares the performance of our method against ShortGPT and TinyFusion across various metrics at token pruning ratios of 33%, 50%, and 67%. The results show our approach surpassing TinyFusion (Fang et al. 2024) and ShortGPT (Men et al. 2024) at every pruning ratio, which demonstrates its robust ability to recover performance. Furthermore, the model exhibits only a slight degradation in performance as the pruning ratio is increased from 33% to 50%, indicating the continued presence of parameter redundancy at the 33% level. However, as the pruning rate increases from 50% to

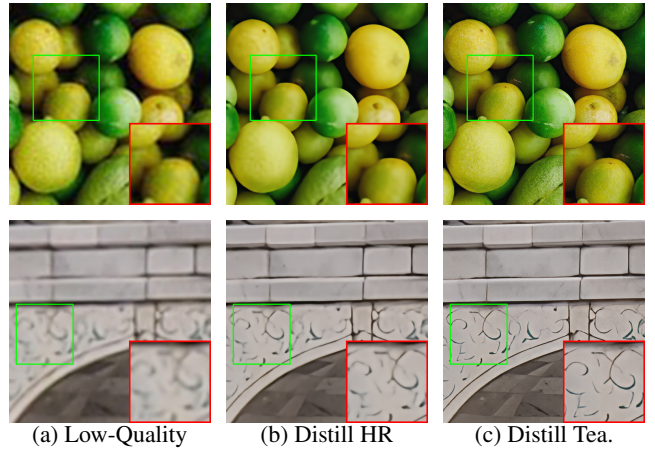


Figure C.2: Visual comparison of knowledge distillation: high-resolution ground truth versus teacher.

Table C.2: Ablation study of pruning ratio on DIV2K-Val dataset. The best is highlighted in **bold**.

Method	Pruning Ratio	LPIPS \downarrow	DISTS \downarrow	NIQE \downarrow	MANIQA \uparrow	CLIPQA \uparrow
ShortGPT	33%	0.3049	0.2150	5.1010	0.5727	0.7248
TinyFusion	33%	0.2808	0.1928	4.3013	0.5912	0.7274
Ours	33%	0.2789	0.1917	4.1396	0.6071	0.7284
ShortGPT	50%	0.2892	0.2034	4.8874	0.5681	0.7116
TinyFusion	50%	0.2799	0.1904	4.1705	0.5880	0.6995
Ours	50%	0.2793	0.1883	4.1500	0.6083	0.7201
ShortGPT	67%	0.3466	0.2476	5.5182	0.5257	0.7069
TinyFusion	67%	0.3071	0.2194	4.7256	0.5217	0.7056
Ours	67%	0.2984	0.2110	4.2475	0.5389	0.7198

67%, the model’s performance on metrics such as DISTS and MANIQA declines sharply, indicating that excessive pruning leads to irreversible performance degradation.

C.3 Ablation Study of Knowledge Distillation

Tab. C.3 demonstrates the effectiveness of our knowledge distillation method under stage 1. We can draw the following conclusions: (1) Distillation employing GT (High-Quality) data consistently resulted in unsatisfactory performance, whether applied in the image space or the latent space. As illustrated in Fig. C.2, distillation using GT data yields smooth, blurred results, whereas using the teacher produces clearer textures. (2) Distillation performed in the image space achieves better scores on full-reference metrics such as SSIM, LPIPS, and DISTS. Distillation in the latent space yields superior no-reference metrics (MUSIQ, CLIPQA, TOPIQ and Q-Align), with most even matching those of the teacher model. However, a potential compromise in reference metrics necessitates a second stage of training, which we perform in the image space.

C.4 Ablation Study of Losses in Stage 2

We conduct an ablation study on the Stage 2 training losses, as shown in Tab. C.4. The results indicate that Stage 2 training significantly improved image quality, particularly in terms of image fidelity. Specifically, we find that the inclusion of LPIPS loss is highly beneficial for improving reference metrics such as DISTS and FID. The addition of GAN loss, in

Table C.3: Ablation studies of Stage 1 distillation loss on DrealSR dataset. The best (other than Teacher) is highlighted in **bold**.

Method	SSIM \uparrow	LPIPS \downarrow	DISTS \downarrow	FID \downarrow	MUSIQ \uparrow	CLIPQA \uparrow	TOPIQ \uparrow	Q-Align \uparrow
Teacher TSD-SR Baseline	0.7559	0.2967	0.2136	134.98	66.62	0.7344	0.6177	3.6055
Distill HR in Image Space	0.8480	0.3082	0.2438	176.50	48.89	0.3456	0.3652	2.4315
Distill TEA. in Image Space	0.7904	0.2819	0.2150	154.16	64.74	0.6171	0.6020	3.2871
Distill HR in Latent Space	0.7814	0.4253	0.2988	190.11	48.41	0.4441	0.4726	2.3841
Distill TEA. in Latent Space (Ours)	0.7508	0.3316	0.2322	148.63	66.57	0.7321	0.6211	3.5356

Table C.4: Ablation studies of Stage 2 training loss on RealSR dataset. The best is highlighted in **bold**.

Method	LPIPS \downarrow	DISTS \downarrow	NIQE \downarrow	MANIQA \uparrow	FID \downarrow
Stage 1 Baseline	0.3087	0.2302	5.1740	0.6045	132.53
w/ LPIPS loss & w/o GAN	0.2702	0.2180	5.0696	0.5850	123.43
w/ GAN loss & w/o LPIPS	0.2844	0.2173	4.7203	0.6073	124.22
w/ LPIPS & w/ GAN (Ours)	0.2806	0.2123	4.7400	0.6235	118.01

turn, is helpful for enhancing several no-reference metrics, including NIQE and MANIQA. We ultimately weighted the two new losses to balance the trade-off between fidelity and the generative ability.

References

Agustsson, E.; and Timofte, R. 2017. Ntire 2017 challenge on single image super-resolution: Dataset and study. In *Proceedings of the IEEE conference on computer vision and pattern recognition workshops*, 126–135.

Bohan, O. B. 2023. Tiny AutoEncoder for Stable Diffusion. <https://github.com/madebyollin/taesd>.

Cai, J.; Zeng, H.; Yong, H.; Cao, Z.; and Zhang, L. 2019. Toward real-world single image super-resolution: A new benchmark and a new model. In *Proceedings of the IEEE/CVF international conference on computer vision*, 3086–3095.

Castells, T.; Song, H.-K.; Kim, B.-K.; and Choi, S. 2024. Ld-pruner: Efficient pruning of latent diffusion models using task-agnostic insights. In *Proceedings of the IEEE/CVF Conference on Computer Vision and Pattern Recognition*, 821–830.

Chen, B.; Li, G.; Wu, R.; Zhang, X.; Chen, J.; Zhang, J.; and Zhang, L. 2024a. Adversarial diffusion compression for real-world image super-resolution. *arXiv preprint arXiv:2411.13383*.

Chen, C.; Mo, J.; Hou, J.; Wu, H.; Liao, L.; Sun, W.; Yan, Q.; and Lin, W. 2024b. Topiq: A top-down approach from semantics to distortions for image quality assessment. *IEEE Transactions on Image Processing*, 33: 2404–2418.

Chen, C.; Shi, X.; Qin, Y.; Li, X.; Han, X.; Yang, T.; and Guo, S. 2022. Real-world blind super-resolution via feature matching with implicit high-resolution priors. In *Proceedings of the 30th ACM International Conference on Multimedia*, 1329–1338.

Chen, J.; Hu, D.; Huang, X.; Coskun, H.; Sahni, A.; Gupta, A.; Goyal, A.; Lahiri, D.; Singh, R.; Idelbayev, Y., et al. 2025. Snapgen: Taming high-resolution text-to-image models for mobile devices with efficient architectures and training. In *Proceedings of the Computer Vision and Pattern Recognition Conference*, 7997–8008.

Chollet, F. 2017. Xception: Deep learning with depthwise separable convolutions. In *Proceedings of the IEEE conference on computer vision and pattern recognition*, 1251–1258.

Daniel Verdú, J. M. 2024. Flux.1 Lite: Distilling Flux1.dev for Efficient Text-to-Image Generation.

Dao, T.; Fu, D.; Ermon, S.; Rudra, A.; and Ré, C. 2022. Flashattention: Fast and memory-efficient exact attention with io-awareness. *Advances in neural information processing systems*, 35: 16344–16359.

Ding, K.; Ma, K.; Wang, S.; and Simoncelli, E. P. 2020. Image quality assessment: Unifying structure and texture similarity. *IEEE transactions on pattern analysis and machine intelligence*, 44(5): 2567–2581.

Dong, L.; Fan, Q.; Guo, Y.; Wang, Z.; Zhang, Q.; Chen, J.; Luo, Y.; and Zou, C. 2025. Tsd-sr: One-step diffusion with target score distillation for real-world image super-resolution. In *Proceedings of the Computer Vision and Pattern Recognition Conference*, 23174–23184.

Esser, P.; Kulal, S.; Blattmann, A.; Entezari, R.; Müller, J.; Saini, H.; Levi, Y.; Lorenz, D.; Sauer, A.; Boesel, F.; et al. 2024. Scaling rectified flow transformers for high-resolution image synthesis. In *Forty-first International Conference on Machine Learning*.

Fang, G.; Li, K.; Ma, X.; and Wang, X. 2024. TinyFusion: Diffusion Transformers Learned Shallow. *arXiv preprint arXiv:2412.01199*.

Han, S.; Pool, J.; Tran, J.; and Dally, W. 2015. Learning both weights and connections for efficient neural network. *Advances in neural information processing systems*, 28.

He, Y.; Liu, L.; Liu, J.; Wu, W.; Zhou, H.; and Zhuang, B. 2023. Ptqd: Accurate post-training quantization for diffusion models. *arXiv preprint arXiv:2305.10657*.

Heusel, M.; Ramsauer, H.; Unterthiner, T.; Nessler, B.; and Hochreiter, S. 2017. Gans trained by a two time-scale update rule converge to a local nash equilibrium. *Advances in neural information processing systems*, 30.

Ho, J.; Jain, A.; and Abbeel, P. 2020. Denoising diffusion probabilistic models. *Advances in neural information processing systems*, 33: 6840–6851.

Howard, A. G.; Zhu, M.; Chen, B.; Kalenichenko, D.; Wang, W.; Weyand, T.; Andreetto, M.; and Adam, H. 2017. Mobiilenets: Efficient convolutional neural networks for mobile vision applications. *arXiv preprint arXiv:1704.04861*.

Jang, E.; Gu, S.; and Poole, B. 2016. Categorical reparameterization with gumbel-softmax. *arXiv preprint arXiv:1611.01144*.

Karras, T.; Laine, S.; and Aila, T. 2019. A style-based generator architecture for generative adversarial networks. In *Proceedings of the IEEE/CVF conference on computer vision and pattern recognition*, 4401–4410.

Ke, J.; Wang, Q.; Wang, Y.; Milanfar, P.; and Yang, F. 2021. Musiq: Multi-scale image quality transformer. In *Proceedings of the IEEE/CVF international conference on computer vision*, 5148–5157.

Kim, B.-K.; Song, H.-K.; Castells, T.; and Choi, S. 2024. Bk-sdm: A lightweight, fast, and cheap version of stable diffusion. In *European Conference on Computer Vision*, 381–399. Springer.

Li, X.; Liu, Y.; Lian, L.; Yang, H.; Dong, Z.; Kang, D.; Zhang, S.; and Keutzer, K. 2023a. Q-diffusion: Quantizing diffusion models. In *Proceedings of the IEEE/CVF International Conference on Computer Vision*, 17535–17545.

Li, Y.; Wang, H.; Jin, Q.; Hu, J.; Chemerys, P.; Fu, Y.; Wang, Y.; Tulyakov, S.; and Ren, J. 2023b. Snapfusion: Text-to-image diffusion model on mobile devices within two seconds. *Advances in Neural Information Processing Systems*, 36: 20662–20678.

Li, Y.; Zhang, K.; Liang, J.; Cao, J.; Liu, C.; Gong, R.; Zhang, Y.; Tang, H.; Liu, Y.; Demandolx, D.; et al. 2023c. Lsdir: A large scale dataset for image restoration. In *Proceedings of the IEEE/CVF Conference on Computer Vision and Pattern Recognition*, 1775–1787.

Liang, J.; Zeng, H.; and Zhang, L. 2022. Details or artifacts: A locally discriminative learning approach to realistic image super-resolution. In *Proceedings of the IEEE/CVF Conference on Computer Vision and Pattern Recognition*, 5657–5666.

Lin, X.; He, J.; Chen, Z.; Lyu, Z.; Dai, B.; Yu, F.; Ouyang, W.; Qiao, Y.; and Dong, C. 2023. Diffbir: Towards blind image restoration with generative diffusion prior. *arXiv preprint arXiv:2308.15070*.

Men, X.; Xu, M.; Zhang, Q.; Wang, B.; Lin, H.; Lu, Y.; Han, X.; and Chen, W. 2024. Shortgpt: Layers in large language models are more redundant than you expect. *arXiv preprint arXiv:2403.03853*.

Nichol, A. Q.; and Dhariwal, P. 2021. Improved denoising diffusion probabilistic models. In *International conference on machine learning*, 8162–8171. PMLR.

Peebles, W.; and Xie, S. 2023. Scalable diffusion models with transformers. In *Proceedings of the IEEE/CVF international conference on computer vision*, 4195–4205.

Rombach, R.; Blattmann, A.; Lorenz, D.; Esser, P.; and Ommer, B. 2022. High-resolution image synthesis with latent diffusion models. In *Proceedings of the IEEE/CVF conference on computer vision and pattern recognition*, 10684–10695.

Shi, W.; Caballero, J.; Huszár, F.; Totz, J.; Aitken, A. P.; Bishop, R.; Rueckert, D.; and Wang, Z. 2016. Real-time single image and video super-resolution using an efficient sub-pixel convolutional neural network. In *Proceedings of the IEEE conference on computer vision and pattern recognition*, 1874–1883.

Teng, Y.; Wu, Y.; Shi, H.; Ning, X.; Dai, G.; Wang, Y.; Li, Z.; and Liu, X. 2024. Dim: Diffusion mamba for efficient high-resolution image synthesis. *arXiv preprint arXiv:2405.14224*.

Timofte, R.; Agustsson, E.; Van Gool, L.; Yang, M.-H.; and Zhang, L. 2017. Ntire 2017 challenge on single image super-resolution: Methods and results. In *Proceedings of the IEEE conference on computer vision and pattern recognition workshops*, 114–125.

Wang, J.; Chan, K. C.; and Loy, C. C. 2023. Exploring clip for assessing the look and feel of images. In *Proceedings of the AAAI conference on artificial intelligence*, volume 37, 2555–2563.

Wang, J.; Yue, Z.; Zhou, S.; Chan, K. C.; and Loy, C. C. 2024a. Exploiting diffusion prior for real-world image super-resolution. *International Journal of Computer Vision*, 1–21.

Wang, X.; Xie, L.; Dong, C.; and Shan, Y. 2021. Real-esrgan: Training real-world blind super-resolution with pure synthetic data. In *Proceedings of the IEEE/CVF international conference on computer vision*, 1905–1914.

Wang, Y.; Yang, W.; Chen, X.; Wang, Y.; Guo, L.; Chau, L.-P.; Liu, Z.; Qiao, Y.; Kot, A. C.; and Wen, B. 2024b. SinSR: diffusion-based image super-resolution in a single step. In *Proceedings of the IEEE/CVF Conference on Computer Vision and Pattern Recognition*, 25796–25805.

Wang, Z.; Bovik, A. C.; Sheikh, H. R.; and Simoncelli, E. P. 2004. Image quality assessment: from error visibility to structural similarity. *IEEE transactions on image processing*, 13(4): 600–612.

Wang, Z.; Jiang, Y.; Zheng, H.; Wang, P.; He, P.; Wang, Z.; Chen, W.; Zhou, M.; et al. 2023. Patch diffusion: Faster and more data-efficient training of diffusion models. *Advances in neural information processing systems*, 36: 72137–72154.

Wei, P.; Xie, Z.; Lu, H.; Zhan, Z.; Ye, Q.; Zuo, W.; and Lin, L. 2020. Component divide-and-conquer for real-world image super-resolution. In *Computer Vision–ECCV 2020: 16th European Conference, Glasgow, UK, August 23–28, 2020, Proceedings, Part VIII 16*, 101–117. Springer.

Wu, H.; Zhang, Z.; Zhang, W.; Chen, C.; Liao, L.; Li, C.; Gao, Y.; Wang, A.; Zhang, E.; Sun, W.; et al. 2023. Q-align: Teaching lmms for visual scoring via discrete text-defined levels. *arXiv preprint arXiv:2312.17090*.

Wu, R.; Sun, L.; Ma, Z.; and Zhang, L. 2024a. One-Step Effective Diffusion Network for Real-World Image Super-Resolution. *arXiv preprint arXiv:2406.08177*.

Wu, R.; Yang, T.; Sun, L.; Zhang, Z.; Li, S.; and Zhang, L. 2024b. Seesr: Towards semantics-aware real-world image super-resolution. In *Proceedings of the IEEE/CVF conference on computer vision and pattern recognition*, 25456–25467.

Xie, R.; Tai, Y.; Zhang, K.; Zhang, Z.; Zhou, J.; and Yang, J. 2024. AddSR: Accelerating Diffusion-based Blind Super-Resolution with Adversarial Diffusion Distillation. *arXiv preprint arXiv:2404.01717*.

Yang, S.; Wu, T.; Shi, S.; Lao, S.; Gong, Y.; Cao, M.; Wang, J.; and Yang, Y. 2022. Maniqa: Multi-dimension attention

network for no-reference image quality assessment. In *Proceedings of the IEEE/CVF Conference on Computer Vision and Pattern Recognition*, 1191–1200.

Yu, F.; Gu, J.; Li, Z.; Hu, J.; Kong, X.; Wang, X.; He, J.; Qiao, Y.; and Dong, C. 2024. Scaling up to excellence: Practicing model scaling for photo-realistic image restoration in the wild. In *Proceedings of the IEEE/CVF Conference on Computer Vision and Pattern Recognition*, 25669–25680.

Yue, Z.; Wang, J.; and Loy, C. C. 2024. Resshift: Efficient diffusion model for image super-resolution by residual shifting. *Advances in Neural Information Processing Systems*, 36.

Zhang, K.; Liang, J.; Van Gool, L.; and Timofte, R. 2021. Designing a practical degradation model for deep blind image super-resolution. In *Proceedings of the IEEE/CVF International Conference on Computer Vision*, 4791–4800.

Zhang, L.; Zhang, L.; and Bovik, A. C. 2015. A feature-enriched completely blind image quality evaluator. *IEEE Transactions on Image Processing*, 24(8): 2579–2591.

Zhang, R.; Isola, P.; Efros, A. A.; Shechtman, E.; and Wang, O. 2018. The unreasonable effectiveness of deep features as a perceptual metric. In *Proceedings of the IEEE conference on computer vision and pattern recognition*, 586–595.